Monthly Notices of the ROYAL ASTRONOMICAL SOCIETY

MNRAS **527,** 7055–7069 (2024) https://doi.org/10.1093/mnras/stad3650
Advance Access publication 2023 November 24

Narrow-line Seyfert 1 galaxies in Sloan Digital Sky Survey: a new optical spectroscopic catalogue

Vaidehi S. Paliya [1]★ C. S. Stalin [2] Alberto Domínguez [3,4] and D. J. Saikia [1]

[1] *Inter-University Centre for Astronomy and Astrophysics (IUCAA), SPPU Campus, Pune 411007, India*
[2] *Indian Institute of Astrophysics, Block II, Koramangala, Bengaluru 560034, Karnataka, India*
[3] *Instituto de Física de Partículas y del Cosmos (IPARCOS), Universidad Complutense de Madrid, E-28040 Madrid, Spain*
[4] *Departamento de Estructura de la Materia, Física Térmica y Electrónica, Universidad Complutense de Madrid, E-28040 Madrid, Spain*

Accepted 2023 November 21. Received 2023 November 21; in original form 2023 June 5

ABSTRACT

Narrow-line Seyfert 1 (NLSy1) galaxies are an enigmatic class of active galactic nuclei (AGN) that exhibit peculiar multiwavelength properties across the electromagnetic spectrum. For example, these sources have allowed us to explore the innermost regions of the central engine of AGN using X-ray observations and have also provided clues about the origin of relativistic jets considering radio and gamma-ray bands. Keeping in mind the ongoing and upcoming wide-field, multifrequency sky surveys, we present a new catalogue of NLSy1 galaxies. This was done by carrying out a detailed decomposition of >2 million optical spectra of quasars and galaxies from the Sloan Digital Sky Survey Data Release 17 (SDSS-DR17) using the publicly available software 'Bayesian AGN Decomposition Analysis for SDSS Spectra'. The catalogue contains 22656 NLSy1 galaxies which is more than twice the size of the previously identified NLSy1s based on SDSS-DR12. As a corollary, we also release a new catalogue of 52273 broad-line Seyfert 1 (BLSy1) galaxies. The estimated optical spectral parameters and derived quantities confirm the previously known finding of NLSy1 galaxies being AGN powered by highly accreting, low-mass black holes. We conclude that this enlarged sample of NLSy1 and BLSy1 galaxies will enable us to explore the low-luminosity end of the AGN population by effectively utilizing the sensitive, high-quality observations delivered by ongoing/upcoming wide-field sky surveys. The catalogue has been made public at https://www.ucm.es/blazars/seyfert.

Key words: techniques: spectroscopic – galaxies: active – galaxies: Seyfert.

1 INTRODUCTION

Narrow-line Seyfert 1 (NLSy1) galaxies were, initially defined as, low-luminosity active galactic nuclei (AGN, absolute *B*-band magnitude $M_B > -23$; Schmidt & Green 1983) which were identified purely based on their optical spectroscopic properties. Osterbrock & Pogge (1985) originally proposed to classify them based on the presence of narrow 'broad permitted lines' and the strength of the forbidden [O III] emission line compared to H β line with flux ratio of [O III] λ5007/H β<3. The spectropolarimetric study of NLSy1 galaxies was later carried out by Goodrich (1989) who quantified the first selection criterion of Osterbrock & Pogge (1985) with the full width at half-maximum (FWHM) of the broad H β line to be <2000 km s^{-1}. These objects exhibit several peculiar observational features such as the strong permitted Fe II complexes, steep soft X-ray spectra, rapid X-ray flux variations (cf. Boller, Brandt & Fink 1996; Leighly 1999a, b) and strong outflows (e.g. Boroson 2002; Komossa et al. 2008; Grupe et al. 2010; Xu et al. 2012). These observations have indicated the existence of rapidly accreting, low-mass black hole systems ($M_{BH} \sim 10^{6-8}\ M_\odot$) powering these enigmatic AGN (e.g. Peterson et al. 2000; Grupe & Mathur 2004; Xu et al. 2012). However, alternative theoretical models have also been put forward by attributing the observed characteristics of NLSy1 galaxies to geometrical parameters, e.g. covering factor, leading to the proposition that NLSy1 source population has been preferentially viewed at small angles compared to their broad-line counterparts (cf. Decarli et al. 2008).

NLSy1 galaxies have been used to study a variety of AGN physics problems. For example, the first fundamental correlation vector or the eigenvector 1 of Type 1 AGN (EV1) which represents the correlations of various observables such as the steep X-ray spectrum or strength of the [O III] or optical Fe II emission with the H β line width, has been argued to be an important Type 1 AGN unification scheme found so far (Boroson & Green 1992; Sulentic, Marziani & Dultzin-Hacyan 2000). These objects have been found to lie at the extreme negative end of EV1 thereby providing us clues about the central engine parameters, e.g. black hole mass or accretion rate, and/or geometrical aspects such as the viewing angle (cf. Boller, Brandt & Fink 1996; Sulentic, Marziani & Dultzin-Hacyan 2000; Marziani et al. 2001). Furthermore, the X-ray spectra of NLSy1 galaxies often show a strong soft X-ray excess and reflection dominated hard X-ray emission (e.g. Fabian et al. 2009). Deep X-ray observations of these sources have permitted us to study the behaviour of matter and energy and their possible interaction in the immediate vicinity of the central supermassive black hole (Parker et al. 2014; Kara et al. 2017). Though

★ E-mail: vaidehi.s.paliya@gmail.com

most of the NLSy1 galaxies are radio-quiet, ∼5 per cent of them are found to be radio-loud indicating the presence of jets (Komossa et al. 2006; Yuan et al. 2008). Some of the very radio-loud NLSy1s have also been detected in the all-sky gamma-ray survey being conducted with the *Fermi*-Large Area Telescope (Abdo et al. 2009; Paliya et al. 2018). This has led to the idea of them being the nascent blazars (e.g. Paliya et al. 2020). Indeed, the general NLSy1 population has been considered as rapidly accreting, low-luminosity AGN in the early stage of their evolution (cf. Mathur 2000; Berton et al. 2018). Moreover, these sources have also been reported to exhibit rapidly rising and long-lasting optical flaring activity thereby making them crucial targets in the era of time-domain astronomy (Frederick et al. 2021).

The above-mentioned research problems highlight the pivotal role that NLSy1 galaxies can play in advancing our current understanding of AGN science. Also considering the latest and upcoming wide-field, multifrequency sky surveys and missions, e.g. Very Large Array Sky Survey (VLASS; Lacy et al. 2020), *eROSITA* (Predehl et al. 2021), and Rubin observatory (Ivezić et al. 2019), it is imperative to increase the sample size of the known NLSy1 galaxies. The latest catalogue of this class of AGN was prepared using the Sloan Digital Sky Survey data release 12 (SDSS-DR12) and contains 11 101 NLSy1s (Rakshit et al. 2017) which superseded the earlier catalogues containing 150 and 2011 sources using SDSS early data release and SDSS-DR3, respectively (Williams, Pogge & Mathur 2002; Zhou et al. 2006). Since then, there have been a number of major updates, both in data collection and analysis software, that motivated us to prepare a new sample of these enigmatic AGN. We highlight a few such updates below:

(i) The number of spectroscopically observed sources has considerably increased in the most recent DR17 which is the final survey from the fourth phase of SDSS (Blanton et al. 2017). For example, SDSS-DR16 contains 750 414 quasars[1] (Lyke et al. 2020) which is more than two times larger than the 297 301 objects published in DR12 (Pâris et al. 2017).

(ii) The work of Rakshit et al. (2017) only considered objects classified as quasars (SDSS pipeline keyword `QSO`). In addition to quasars, we have searched for NLSy1s among ∼1.9 million sources identified as galaxies by the SDSS data reduction pipeline (keyword `GALAXIES`).

(iii) In Rakshit et al. (2017), the analysis of SDSS spectra was done using a custom-built private software. In this work, we have instead adopted the publicly available optical spectroscopic data analysis software 'Bayesian AGN Decomposition Analysis for SDSS Spectra[2]' (BADASS; Sexton et al. 2021). This package is an open-source spectral analysis tool designed for detailed decomposition of SDSS spectra.

(iv) Analysing SDSS spectra with the motivation to identify NLSy1 galaxies will naturally lead to finding new broad-line Seyfert 1 (BLSy1) galaxies. While earlier studies have only reported the NLSy1 galaxy sample (Williams, Pogge & Mathur 2002; Zhou et al. 2006; Rakshit et al. 2017), we release the catalogues of both NLSy1 and BLSy1 sources.

In Section 2, we briefly describe the sample selection criteria, while details of the BADASS spectroscopic data analysis steps are elaborated in Section 3. The new catalogue of NLSy1 galaxies and their multiwavelength properties are discussed in Sections 4 and 5, respectively. We summarize our findings in Section 6. Throughout, a flat cosmology with $H_0 = 70$ km s^{-1} Mpc^{-1} and $\Omega_M = 0.3$ was adopted.

2 SAMPLE SELECTION

We considered all DR-17 sources that were classified either as `QSO` (1370 779 objects) or `GALAXIES` (3237 535 sources) by the SDSS pipeline. Next, we applied the following filters to retain sources for spectroscopic analysis:

(i) reject all sources with z >0.8 and >0.9 for SDSS and Baryon Oscillation Spectroscopic Survey (BOSS) spectrographs, respectively. This is because the optical spectra taken with the BOSS spectrographs have larger wavelength coverage compared to the SDSS spectrographs. This redshift cut ensured that both Hβ and [O III] emission lines, needed to characterize an NLSy1 galaxy, are present in the optical spectrum.

(ii) reject all objects with the keyword `zWarning` >0 and `zWarning` $\neq$ 16. The latter condition, i.e. `zWarning` = 16, usually indicates a high signal-to-noise (S/N) spectrum or broad emission lines in a galaxy.[3]

(iii) reject all sources with the keyword `specprimary` = 0 since the best observations of all unique objects have `specprimary` >0.

(iv) reject all objects with median S/N ratio `snMedianAll` <2.

This exercise left us with 111 506 `QSO` and 1918 262 `GALAXIES`. Furthermore, we also included 11 754 quasars from the SDSS-DR16 quasar catalogue that were left out possibly due to one/more filters mentioned above. Recently, Wu & Shen (2022) reported the results of the optical spectroscopic analysis of SDSS-DR16 quasars and also provided improved redshifts measurements. We used their redshift measurements for sources common in both samples and adopted the SDSS pipeline redshift for the rest of them. Overall, our final sample contains 123 260 quasars and 1918 262 galaxies. The analyses of these >2 million spectra were carried out using BADASS software as described in the next section.

3 OPTICAL SPECTROSCOPIC DATA ANALYSIS

3.1 Bayesian AGN decomposition analysis for SDSS spectra

BADASS is an open source optical spectroscopic data analysis package designed to automate the deconvolution of AGN and host galaxy spectra, simultaneously fitting both emission line and continuum features, and estimating robust parameter uncertainties using Markov Chain Monte Carlo (MCMC) approach. The full description of the tool can be found in Sexton et al. (2021, 2022) and here we summarize its salient features.

In the first step, the optical spectrum is brought to the rest-frame and corrected for the Galactic extinction using the extinction map of Schlafly & Finkbeiner (2011) and extinction law of Cardelli, Clayton & Mathis (1989) considering $R_V = 3.1$. Next, the software simultaneously fits all components, e.g. emission lines, to constrain their relative contribution and covariances.

To model the continuum emission, BADASS uses a composite host-galaxy template (e.g. Vazdekis et al. 2016) or empirical stellar templates to estimate the line-of-sight velocity distribution (cf. Cappellari 2017), a power law and Balmer pseudocontinuum components mimicking the AGN contribution (cf. Dietrich et al. 2002),

[1] SDSS-DR-17 does not contain any new spectroscopically observed quasars.
[2] https://github.com/remingtonsexton/BADASS3
[3] https://www.sdss4.org/dr17/algorithms/bitmasks/#ZWARNING

and optical-ultraviolet Fe II emission (Vestergaard & Wilkes 2001; Véron-Cetty, Joly & Véron 2004).

The BADASS software provides several line profile shapes, e.g. Gaussian or Lorentzian, to fit the broad and narrow emission lines. The measured line widths are corrected for the SDSS instrumental resolution. The flux ratios of [O III] and [N II] doublets are kept fixed to three during the fit (e.g. Shen et al. 2011). Optionally, the widths of narrow lines can also be tied, e.g. all narrow-line width components in the H β region are tied to the [O III] line width.

The model fitting in BADASS is done using the Bayesian affine-invariant MCMC sampler EMCEE (Foreman-Mackey et al. 2013). To obtain the initial parameter values, a maximum-likelihood fit is performed adopting a Gaussian likelihood distribution. The full parameter space is then scanned using MCMC to derive robust parameter and uncertainty estimates. Additionally, the software also provides an option of performing multiple iterations of maximum-likelihood fitting by applying a Monte Carlo bootstrapping technique. The spectra are perturbed by adding a random normally distributed noise at every pixel using the spectral flux uncertainties and re-fitting the spectra. The median (50th percentile) of the distribution is adopted as the best-fitting values of the spectral parameters and the semi amplitude of the range covering the 16th–84th percentiles of the distributions is considered as 1σ uncertainties on each parameter.

3.2 Spectral analysis of quasars

The spectral fitting of 123 260 SDSS quasars was done in the wavelength range 3500–7000 Å. The host galaxy emission was modelled with three single stellar population templates of ages 0.1, 1, and 10 Gyr from EMILES library (Vazdekis et al. 2016). We did not attempt applying more sophisticated penalized Pixel-Fitting software (PPXF; Cappellari 2017) to model the host galaxy emission since the overall spectrum is expected to be dominated by the emission lines. To reproduce the continuum, we also considered a power law and optical Fe II complex template from Véron-Cetty, Joly & Véron (2004). Since Balmer lines in NLSy1 galaxies are usually better represented by a Lorentzian function (cf. Sulentic et al. 2002; Goad, Korista & Ruff 2012; Cracco et al. 2016), we fitted the broad components of H α and H β emission lines with a Lorentzian function. The narrow emission line profiles, on the other hand, were modelled with a Gaussian function. The [O III] doublet was fitted with a single or double Gaussian functions, one each for the core and wing, depending on the line shapes and S/N ratio of the data. We also applied the condition that the width of the broad components must be larger than that of the narrow emission lines. A maximum-likelihood fitting technique using a normal likelihood distribution was adopted to carry out the initial optimization of the spectral parameters which was followed by MCMC fitting for the robust parameter and uncertainty estimations. A maximum of 5000 iterations of MCMC sampling were performed with 100 walkers per parameter and we considered the final 1000 iterations (4000 burn-in) for the posterior distributions. The median of the distribution was taken as the best-fitting value and the 16th and 84th percentiles of the distributions were used as the lower- and upper-bound 1σ uncertainties on each measured quantity. Fig. 1 shows the fitted optical spectrum of one of the analysed quasars.

3.3 Spectral analysis of galaxies

The optical spectral analysis of ∼1.9 million SDSS galaxies was carried out following a strategy similar to that adopted to model the quasar spectra. However, given the large number of sources and to optimize the computational resources, we divided the analysis in two parts. First, we modelled the continuum with a power law and optical Fe II template and also applied the PPXF software to reproduce the strong host galaxy emission. The emission lines were modelled with Gaussian functions and the S/N ratio of the broad H β emission line was computed. To speed up the process, results obtained from a single maximum-likelihood fitting were considered. At this stage, we rejected all sources in which the S/N ratio of the broad H β emission line was found to be <2. This exercise led to the selection of 1143 galaxies. Then, we repeated the full spectral fitting, similar to that adopted for quasars, on these objects and estimated the parameters and uncertainties by applying the MCMC fitting technique. An example of the fitting is demonstrated in Fig. 1.

3.4 Reliability of spectral modelling

The BADASS software carries out the spectral data analysis in fully automatic mode. As usual for any modelling technique, the reliability of the fitting results strongly depends on the S/N ratio of the spectrum. In Fig. 2, we show the distribution of the S/N ratio of the H β and H α emission line regions. For H β line, majority of sources have S/N ratio ∼5 possibly due to the fact that DR17 quasars probe fainter flux limits compared to previous data releases given the improved sensitivity of BOSS spectrographs (see e.g. Shen et al. 2011; Wu & Shen 2022). In this regard, the application of MCMC fitting that has allowed us to derive the robust parameter uncertainties by properly taking into account the data quality, ensures that the measured parameters are reliable. Unlike the conventionally adopted least-square fitting method which may get stuck to a local minima, MCMC fitting scans the full parameter space so that the global minima is achieved. Furthermore, we also performed a number of checks and cross-matched our results with other published works to verify the robustness of the obtained results as described in the next section. We also provide the S/N ratio measured for all of the broad and narrow emission lines in our NLSy1 and BLSy1 catalogues so that a user can customize the selection of objects for a particular research problem.

4 RESULTS

We derived the emission line parameters for 123 260 quasars and 1143 galaxies using the BADASS software. All fitted spectra were visually inspected to filter out contaminating objects whose spectral parameters could not be well constrained. If required, the fit was repeated, e.g. with modified wavelength coverage to avoid noisy edges of the spectrum, and parameters were calculated again. This led to the rejection of 49 428 optical spectra. A major fraction of these objects turned out to be either Type 2 AGN with no broad lines detected in their optical spectra or those with extremely poor quality data. The spectral parameters of the remaining 74 975 AGN, including 222 galaxies, were further analysed to identify NLSy1 and BLSy1 galaxies as discussed in the next section.

In Fig. 3, we plot some of the measured spectral parameters, namely FWHM and flux of the broad H α and H β components for the full sample. We also show the variation of the FWHM of the broad H β line as a function of the optical Fe II strength (R_{4570}) which is defined as the ratio of the Fe II flux in the wavelength range 4434−4684 Å to the flux of the broad component of the H β emission line (e.g. Boroson & Green 1992). The FWHM of the broad components of the Balmer lines are found to be correlated as $\mathrm{FWHM_{H\alpha}} \propto (0.82 \pm 0.01)\mathrm{FWHM_{H\beta}}$ confirming the results found in earlier studies (cf. Zhou et al. 2006). Similarly, the flux

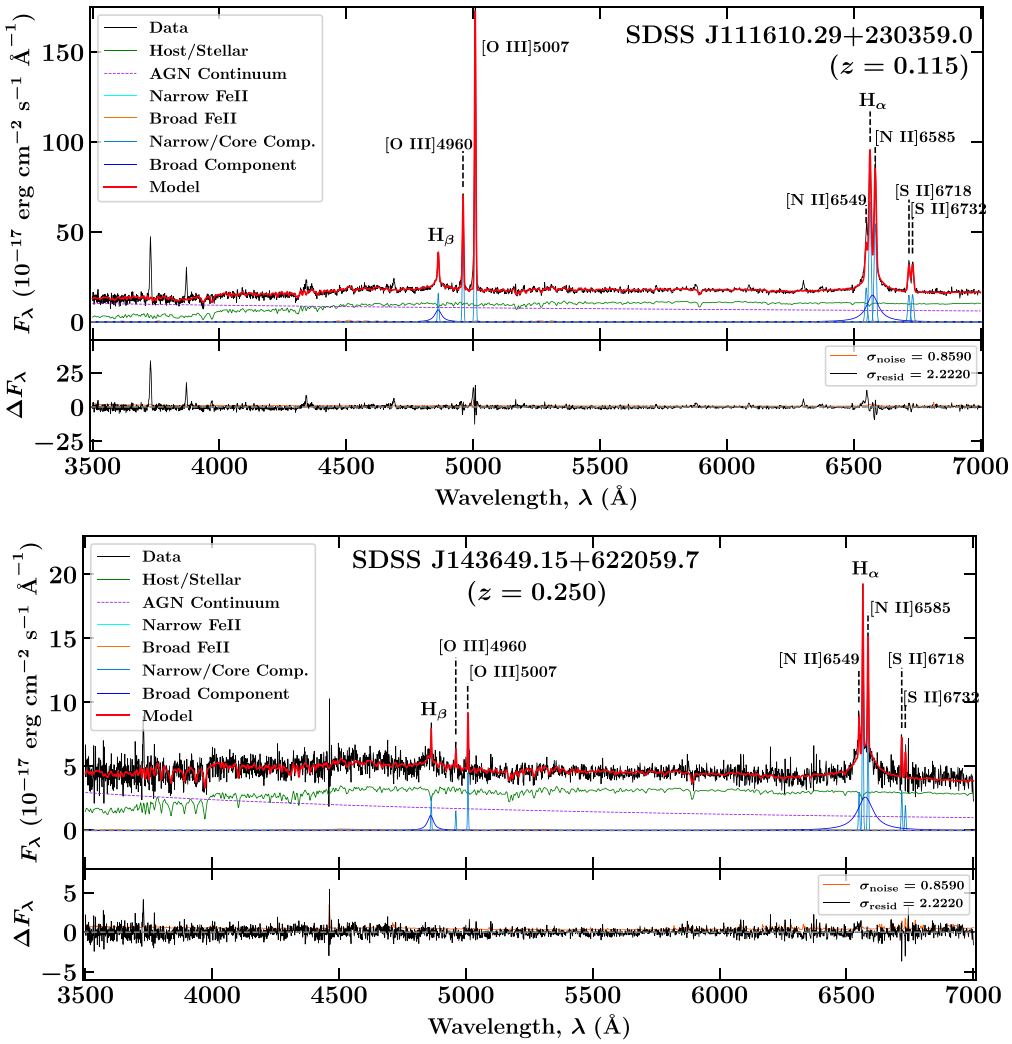

Figure 1. Examples of the spectral fitting of a quasar (top) and a galaxy (bottom) spectra released in SDSS-DR17. The modelled components are labelled.

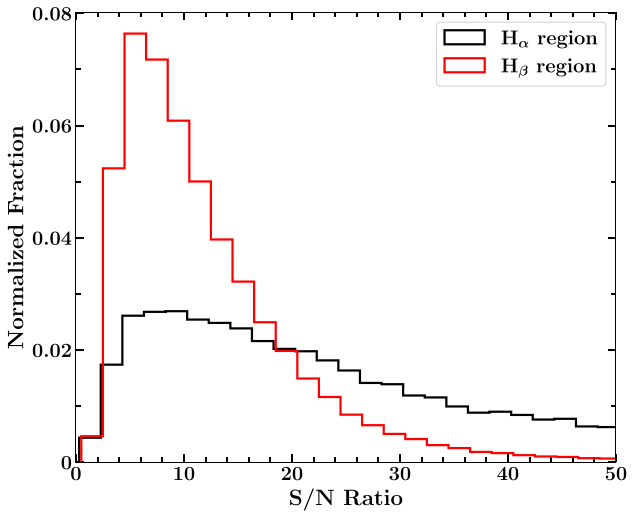

Figure 2. This plot shows the distributions of the measured S/N ratio for the Hα and Hβ regions. The areas of the plotted histograms are normalized to unity.

values of the broad Hα and Hβ lines are also correlated with $F_{H\alpha} \propto (3.41 \pm 0.01) F_{H\beta}$ (e.g. Domínguez et al. 2013).

In Appendix, Table A1 reports the measured spectral parameters for the sample which is published in the form of online NLSy1 and BLSy1 catalogues.[4] Along with the measured quantities, we also derived *B*-band absolute magnitude (M_B), bolometric luminosity (L_{bol}), single epoch virial black hole mass (M_{SE}), and Eddington ratio (R_{Edd}).

We used the SDSS *g* and *r*-filter magnitudes and adopted the following transformation equation to estimate the Bessel *B*-band magnitude (Jordi, Grebel & Ammon 2006):

$$B = g + (0.313 \pm 0.003) * (g - r) + (0.219 \pm 0.002), \quad (1)$$

which was then used to estimate M_B. The objective of calculating this parameter was to consider the fact that most of the studies on NLSy1 galaxies do not differentiate them with narrow-line quasars. Though we also do not apply any selection filter using the absolute magnitude based quasar/Seyfert classification ($M_B \lesssim -23$, Schmidt & Green 1983), this piece of information may enable the user to select genuine

[4] https://www.ucm.es/blazars/seyfert

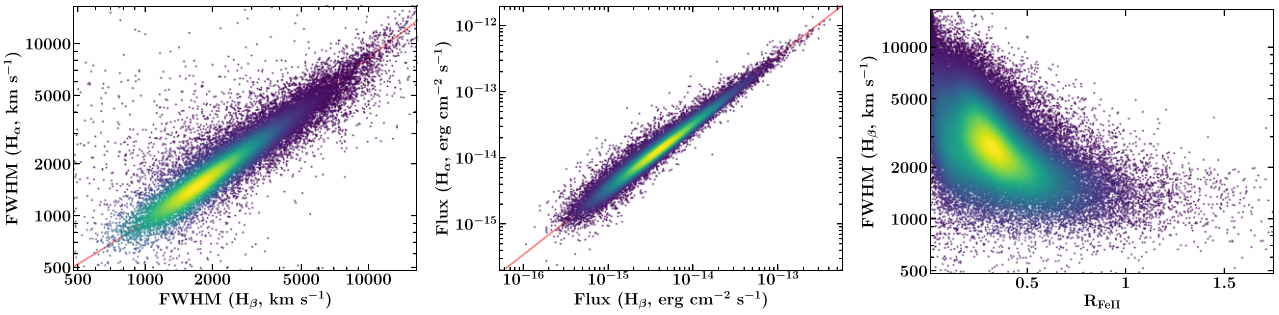

Figure 3. The left and middle panels show the variation of the broad H α emission line FWHM and flux, respectively, with that measured for the broad H β line. The red line refers to the best-fitted correlation for the plotted quantities. The distribution of the sources on the optical Fe II strength versus H β line FWHM plane is shown in the right panel. In all plots, the number density of the data points is colour coded with lighter colours representing larger density of sources.

NLSy1 objects. For the sake of consistency, we throughout mention all broad/narrow-line objects as BLSy1/NLSy1 galaxies.

We considered the commonly adopted single epoch virial technique to estimate the mass of the central black hole that assumes the broad-line region to be virialized (e.g. Vestergaard & Peterson 2006). In particular, the following equation was used to calculate $M_{\rm SE}$ (e.g. McLure & Dunlop 2004):

$$M_{\rm SE} = \frac{\zeta R_{\rm BLR} V_{\rm BLR}^2}{G}, \tag{2}$$

where $V_{\rm BLR}$ is the Keplerian velocity of the line emitting BLR clouds, $R_{\rm BLR}$ is the BLR radius, and G is the gravitational constant. The parameter ζ refers to the scale factor considering the kinematics and geometry of the BLR and taken as $\zeta = 3/4$ assuming spherical distribution of clouds (Rakshit et al. 2017). The $R_{\rm BLR}$ was estimated following Du & Wang (2019) who updated the scaling relation between $R_{\rm BLR}$ and 5100 Å continuum luminosity including the relative strength of Fe II emission, which is important for highly accreting AGN such as NLSy1 galaxies. In particular, the following equation was adopted:

$$\log\left(\frac{R_{\rm BLR}}{\rm lt-day}\right) = A + B\log\left(\frac{\lambda L_{\lambda,5100}}{10^{44}\,{\rm erg\,s^{-1}}}\right) + C\,R_{4570}, \tag{3}$$

where coefficients A, B, and C are estimated as 1.65, 0.45, and −0.35 (Du & Wang 2019). The reported uncertainty in $M_{\rm SE}$ refers to measurement errors and does not take into account any systematics which can be as large as 0.4 dex (e.g. Shen 2013). Furthermore, we computed $L_{\rm bol}$ from 5100 Å continuum luminosity adopting the bolometric correction factor of 9.26 (Richards et al. 2006). The Eddington ratio, $R_{\rm Edd}$, was estimated from the derived $M_{\rm SE}$ and $L_{\rm bol}$.

4.1 The NLSy1 catalogue

To identify the genuine NLSy1 galaxies, we used the following two conditions:

(i) the FWHM of the broad H β emission line within measured uncertainties is smaller than 2000 km s^{-1}, i.e. FWHM − ΔFWHM $\leq$ 2000 km s^{-1}.

(ii) the flux ratio of [O III] λ5007 and H β emission lines within estimated uncertainties is <3, where we propagated the uncertainties in the H β and [O III] λ5007 flux values while computing the ratio.

The first filter follows the classic definition of NLSy1 galaxies (Goodrich 1989). It is slightly different from that used in previous NLSy1 catalogues (cf. Zhou et al. 2006; Rakshit et al. 2017). These works used the H β FWHM threshold of 2200 km s^{-1} without considering the uncertainties in the measured quantity which we have accounted for. The second condition was proposed to separate NLSy1s from Seyfert 2 galaxies. To calculate the ratio, the fluxes of those [O III] λ5007 and narrow H β emission lines were considered that have S/N ratio >1 and non-zero flux uncertainties, otherwise flux values were assumed zero since in such cases the line detection is marginal at best. The application of above two filters led to the final sample of 22 656 NLSy1 galaxies present in SDSS-DR17. There are 46 sources that qualified the first selection filter but not the second, i.e. the flux ratio of [O III] λ5007 and H β emission lines was found to be >3. If the threshold of FWHM of the broad H β component is relaxed to 2200 km s^{-1}, the NLSy1 sample size grows to 27 298. Nevertheless, we stick to the original threshold of 2000 km s^{-1} and list all other objects in the BLSy1 catalogue so that if a user wishes to use the relaxed criterion, they can find all of the information in this catalogue. Furthermore, 17 206 sources have $M_{\rm B} > -23$ indicating a large fraction of the NLSy1 sample to be genuine Seyfert galaxies (Schmidt & Green 1983).

4.2 Comparison with previous works

For a consistency check, we compared our catalogue of NLSy1 galaxies with earlier published works. Cross-matching with the SDSS-DR12 NLSy1 catalogue (Rakshit et al. 2017) by using a maximum search radius of 3 arcsec, we found that 884 quasars classified as NLSy1 galaxies in SDSS-DR12 were rejected during the visual inspection. Among the remaining 10 217 objects, 8904 i.e. ∼87.1 per cent, sources are common in both the catalogues. If we adopt the relaxed threshold of FWHM$_{\rm H\,\beta}$ = 2200 km s^{-1} to select NLSy1s, the match percentage increases to 94.5 per cent with 9650 sources present in both the works. A comparison of the redshift distributions indicates that a majority of the newly identified NLSy1 galaxies in our work are at higher redshifts (Fig. 4).

In Fig. 5, we have shown comparison of some of the parameters derived in the two papers. The FWHM values of the broad H α emission line were found to be similar to that measured for SDSS-DR12 NLSy1 objects. The logarithmic ratio of the measured quantities is -0.04 ± 0.10. A small fraction of the sources appear to be systematically shifted with DR12 measurements having higher values (Fig. 5, top left panel). To investigate the differences, we cross-matched the SDSS-DR12 NLSy1 catalogue with SDSS-DR3 NLSy1 catalogue (Zhou et al. 2006) and compared their measurements of the broad H α FWHM values. The top middle panel of Fig. 5 reveals the comparison where the same pattern can be seen. This observation indicates a possible issue in estimating the broad H α FWHM values for some of the SDSS-DR12 NLSy1 objects. Furthermore,

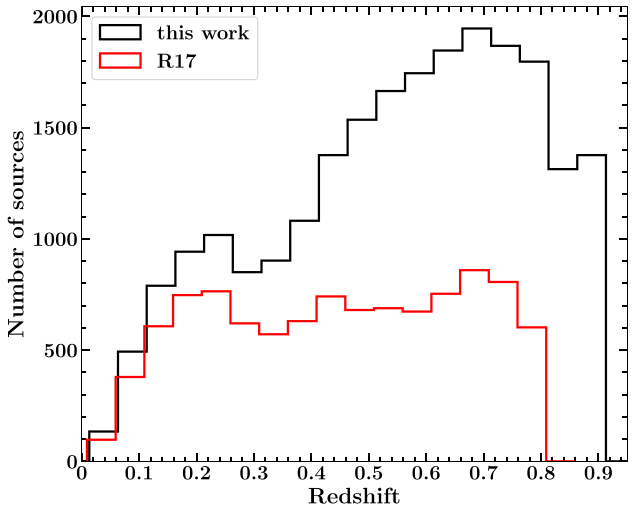

Figure 4. The redshift histograms of NLSy1 galaxies present in our sample and that included in the SDSS-DR12 NLSy1 catalogue.

the broad Hα flux measurements done by us reasonably matches with that published for SDSS-DR12 NLSy1s (average logarithmic ratio 0.06 $\pm$ 0.09, Fig. 5, top right panel). In this diagram also, a small fraction of objects have systematically lower broad Hα flux values as reported in SDSS-DR12 NLSy1 catalogue. These objects turned out to be the same that have systematically offset FWHM of the broad Hα line seen in the top left panel of Fig. 5.

We made an attempt to understand such outliers with larger FWHM and smaller flux values of the broad Hα component reported in the SDSS-DR12 NLSy1 catalogue with respect to our measurements. The fitting of the Hα line region is complex due to the presence of the [N II] $\lambda\lambda$6549, 6585 doublet overlapping with the broad and narrow Hα components. Therefore, one possibility could be due to issues in properly decomposing these emission lines, which can affect the broad Hα measurements. In Fig. 6, we show the spectral fitting results for one of the outliers. The top panel shows the final result derived after running 5000 iterations of the MCMC fitting. We obtained the broad Hα FWHM of 758 km s^{-1} and the flux of 2.9×10^{-14} erg cm^{-2} s^{-1}. The bottom panel shows the fitting result for one of the MCMC iterations where the Hα line was mainly fitted with the narrow Hα component, thereby suppressing the broad Hα component. This led to broader FWHM (1856 km s^{-1}) and lower flux (1.7×10^{-14} erg cm^{-2} s^{-1}) values for the broad Hα component. Indeed, outliers with larger FWHM have lower flux values in the SDSS-DR12 NLSy1 catalogue with respect to our measurements (Fig. 5, top left and right panels). Therefore, it is possible that the Hα line region fitting done by Rakshit et al. (2017) might have found local minima (with fitting solutions similar to the bottom panel of Fig. 6) for such outliers.

We found close matches between broad Hβ flux and FWHM measurements with the logarithmic ratio distribution having an average of 0.06 $\pm$ 0.09 and $-$0.01 $\pm$ 0.10, respectively (Fig. 5, middle left and central panels). The average logarithmic ratio of the [O III] λ5007 line flux measured in this work to that in SDSS-DR12 is 0.04 $\pm$ 0.19. The large dispersion is possibly due to larger scatter seen in fainter sources where two measurements appears to deviate though the overall trend remains the same (Fig. 5, middle right panel). We have also compared the AGN continuum luminosity at 5100 Å and found the results to be similar (logarithmic ratio $-$0.01 $\pm$ 0.21). Finally, a comparison of the Fe II strength, i.e. R_{4570} parameter, reveals our measurements to be slightly higher than that found by Rakshit et al. (2017) for SDSS-DR12 NLSy1 galaxies. The logarithmic ratio of the two measurements is 0.08 $\pm$ 0.18. Altogether, though the spectral modelling strategies of both works are different, the overall results appear similar and we were able to retrieve >80 per cent of SDSS-DR12 NLSy1 galaxies thereby hinting at the robustness of the fitting procedure.

We have also compared our results with the SDSS-DR3 NLSy1 catalogue of 2011 sources (Zhou et al. 2006). There are 23 SDSS-DR3 NLSy1 galaxies which were rejected in our analysis. Among the remaining 1988 objects, 1849, i.e. 93 per cent, were found common in both the works. Adopting the relaxed threshold of $\mathrm{FWHM}_{\mathrm{H}\beta} = 2200$ km s^{-1}, the number of common AGN increases to 1928 i.e. 97 per cent of the SDSS-DR3 NLSy1 galaxies. We show the comparison of various spectral parameters derived in this work and that obtained by Zhou et al. (2006) in Fig. 7. The logarithmic ratio of the FWHM of the broad Hα emission line has an average of 0.01 $\pm$ 0.05 and unlike SDSS-DR12 NLSy1s, there is no significant offset of sources (Fig. 7, top left panel). The flux values of the broad Hα and Hβ emission lines were also similar with the average logarithmic ratio of 0.05 $\pm$ 0.07 and 0.01 $\pm$ 0.08, respectively (Fig. 7, top middle and right panels). The FWHM of the broad Hβ component measured in both the works has an average logarithmic ratio of 0.01 $\pm$ 0.07 indicating a close match (Fig. 7, bottom left panel). Similarly, a comparison of the [O III] λ5007 line flux and Fe II complex strengths reveal the measured values to be very similar with average logarithmic ratio of $-$0.004 $\pm$ 0.160 and 0.05 $\pm$ 0.14, respectively. All these results highlight the accuracy of the adopted fitting technique and the robustness of the derived spectral parameters.

4.3 The BLSy1 catalogue

The BLSy1 catalogue was prepared from the parent sample after removing the NLSy1 galaxies and 46 narrow-line objects that have the flux ratio of [O III] λ5007 and Hβ emission lines >3. The total number of BLSy1 galaxies is 52 273. We caution that it may not be appropriate to consider all of them as genuine Seyfert galaxies since luminous broad-line quasars are also present in the sample. Indeed, dividing the objects based on their M_{B} values, we found 24 401 broad-line sources to be quasars with $M_{\mathrm{B}} < -23$ and 27 761 broad-line Seyferts with absolute B-band magnitude >$-$23 (Schmidt & Green 1983).

5 MULTIWAVELENGTH PROPERTIES

The NLSy1 galaxies exhibit peculiar observational characteristics across the electromagnetic spectrum as outlined in Section 1. Though a detailed multiwavelength study of these sources is beyond the scope of the current work, we briefly describe interesting observational features by cross-matching our catalogues with several multi-frequency catalogues.

5.1 Radio observations

The NLSy1 objects are generally faint radio emitters with only a small fraction (~5 per cent) detected in radio surveys (cf. Komossa et al. 2006; Singh & Chand 2018). We cross-matched our NLSy1 sample with the Faint Images of the Radio Sky at Twenty-Centimeters (FIRST; White et al. 1997) with 5 arcsec search radius and found 730 radio emitting NLSy1 galaxies. Interestingly, though our catalogue is more than two times larger than SDSS-DR12 NLSy1 catalogue, the

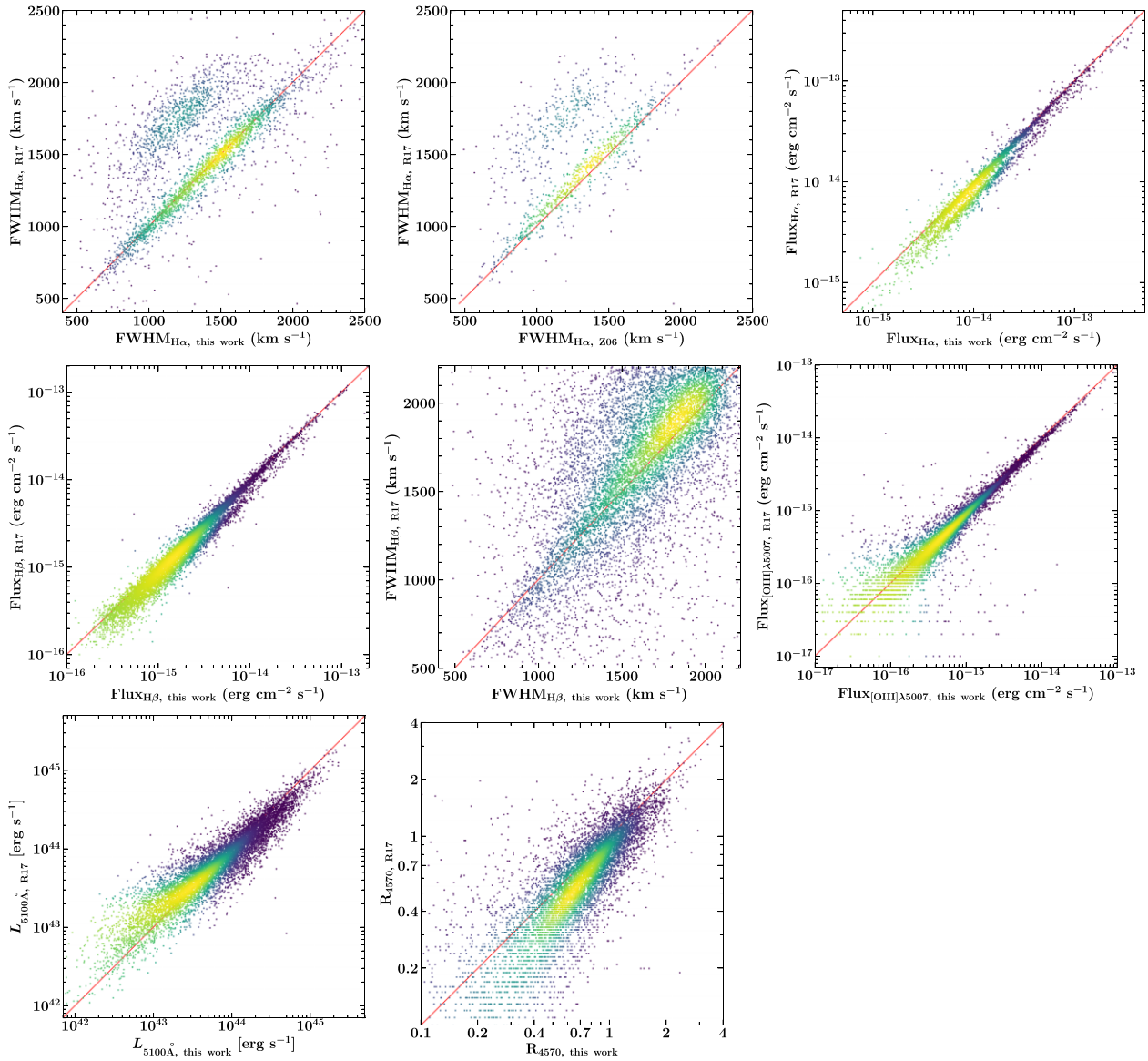

Figure 5. This plot shows the comparison of various spectral parameters obtained in this work and that published for SDSS-DR12 NLSy1 catalogue (R17, Rakshit et al. 2017). The colour coding is done based on the number density of sources. The red line refers to the one-to-one correlation.

number of radio detected sources has increased only by a factor of ∼1.3. The fraction of radio detected NLSy1 galaxies in our sample is ∼3 per cent which is smaller than ∼5 per cent reported for SDSS-DR12 NLSy1 catalogue (Rakshit et al. 2017). This can be understood by considering the fact that the enhancement in the number of NLSy1s is largely at higher redshifts (Fig. 4). If we assume the radio luminosity of the sources to be similar, a higher redshift implies a fainter flux which may remain below the sensitivity of the FIRST survey.

We derived the radio-loudness parameter (R) as the ratio of the rest-frame flux densities at 5 GHz and 4400 Å (Kellermann et al. 1989). The 5 GHz flux density was calculated by extrapolating the 1.4 GHz integrated flux density assuming the spectral index $\alpha = 0.5$ ($F_\nu \propto \nu^{-\alpha}$). Out of the 730 radio detected NLSy1s, 460 are identified as radio-loud ($R > 10$). This fraction (460/730, ∼63 per cent) is smaller than the ∼68 per cent found for SDSS-DR12 NLSy1 objects (Rakshit et al. 2017). The difference in the adopted methods to compute the R parameter in both works could explain this observation. Indeed, Rakshit et al. (2017) calculated it as the ratio of the flux densities at 1.4 GHz and optical g-band flux, whereas, we have used the conventional definition (Kellermann et al. 1989).

The cross-matching of the BLSy1 catalogue with the FIRST survey led to the identification of 2568 radio detected AGN among which 1975, i.e. ∼77 per cent are found to have $R > 10$. On comparing the radio-loudness with that estimated for NLSy1 sample, the overall distributions appear similar (logarithmic dispersion ∼0.9, Fig. 8) though the median average R value for BLSy1s (∼51) is higher than that estimated for NLSy1 galaxies (∼17). Similarly, the distributions of the 1.4 GHz radio power for both populations also have a similar dispersion (∼1.1, on logarithmic scale) though BLSy1 galaxies are more luminous (median average ∼5.7 × 10^{40} erg s^{-1}) compared to NLSy1 sources (∼1.6 × 10^{40} erg s^{-1}). The distributions are plotted in the right panel of Fig. 8.

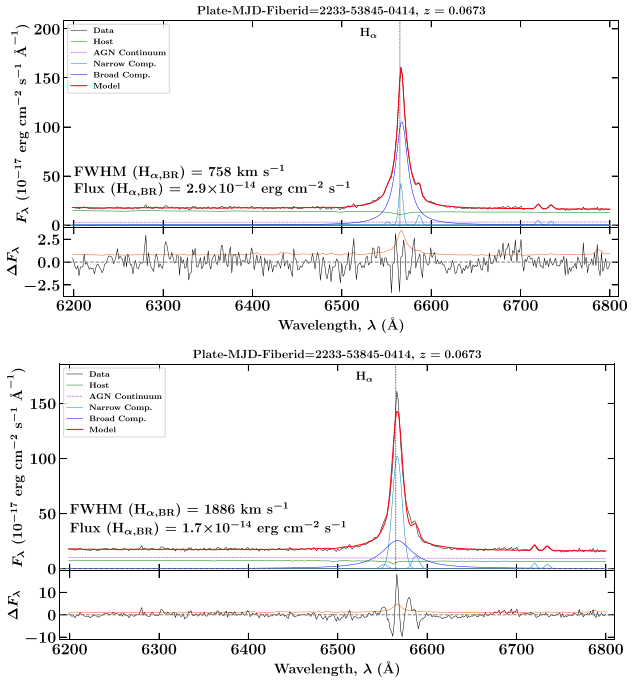

Figure 6. Results of the spectral fitting done on one of the outliers found in Fig. 5, top left panel. The top panel shows the fitting result obtained after 5000 iterations of the MCMC fitting, whereas, the bottom panel refers to that obtained for one of the MCMC iterations. The measured FWHM and flux values for the broad H α component are mentioned. See the text for details.

5.2 Infrared observations

The mid-infrared counterparts of the NLSy1/BLSy1 sources were identified by considering the Wide-field Infrared Survey Explorer (WISE; Wright et al. 2010) catalogue and applying a search radius of 5 arcsec. Out of 22656 NLSy1 objects, 21 825 (∼96 per cent), 21 807 (∼96 per cent), and 18 118 (∼80 per cent) are detected in $W1$, $W2$, and $W3$ filters, respectively, at $>3\sigma$ confidence level. Considering 52 273 BLSy1 galaxies, 51 229 (∼98 per cent), 51 231 (∼98 per cent), and 45 759 (∼88 per cent) are detected in the same bands, respectively.

We show the NLSy1 and BLSy1 objects detected in all three $W1$, $W2$, and $W3$ bands in the WISE colour–colour diagram in Fig. 9. Both BLSy1 and NLSy1s occupy overlapping regions which is found to be dominated by luminous quasars and Seyfert galaxies (cf. Yan et al. 2013; Assef et al. 2018). A small fraction of sources also spread into the region of starburst galaxies.

5.3 Optical observations

A strong correlation between continuum luminosity and emission line luminosities has been reported both for quasar and NLSy1 populations covering a wide range of redshift and bolometric luminosities (Greene & Ho 2005; Zhou et al. 2006; Jun et al. 2015; Rakshit et al. 2017). We show the variations of the H α, H β, and [O III] λ5007 emission line luminosities as a function of the 5100Å continuum luminosity for NLSy1 sources in Fig. 10. The following relations were found by applying a linear least-square fit on the data:

$$\log(L_{\mathrm{H}\beta}) = (1.13 \pm 0.12) + (0.938 \pm 0.002) \log L_{5100}. \quad (4)$$

$$\log(L_{\mathrm{H}\alpha}) = (2.47 \pm 0.17) + (0.917 \pm 0.004) \log L_{5100}. \quad (5)$$

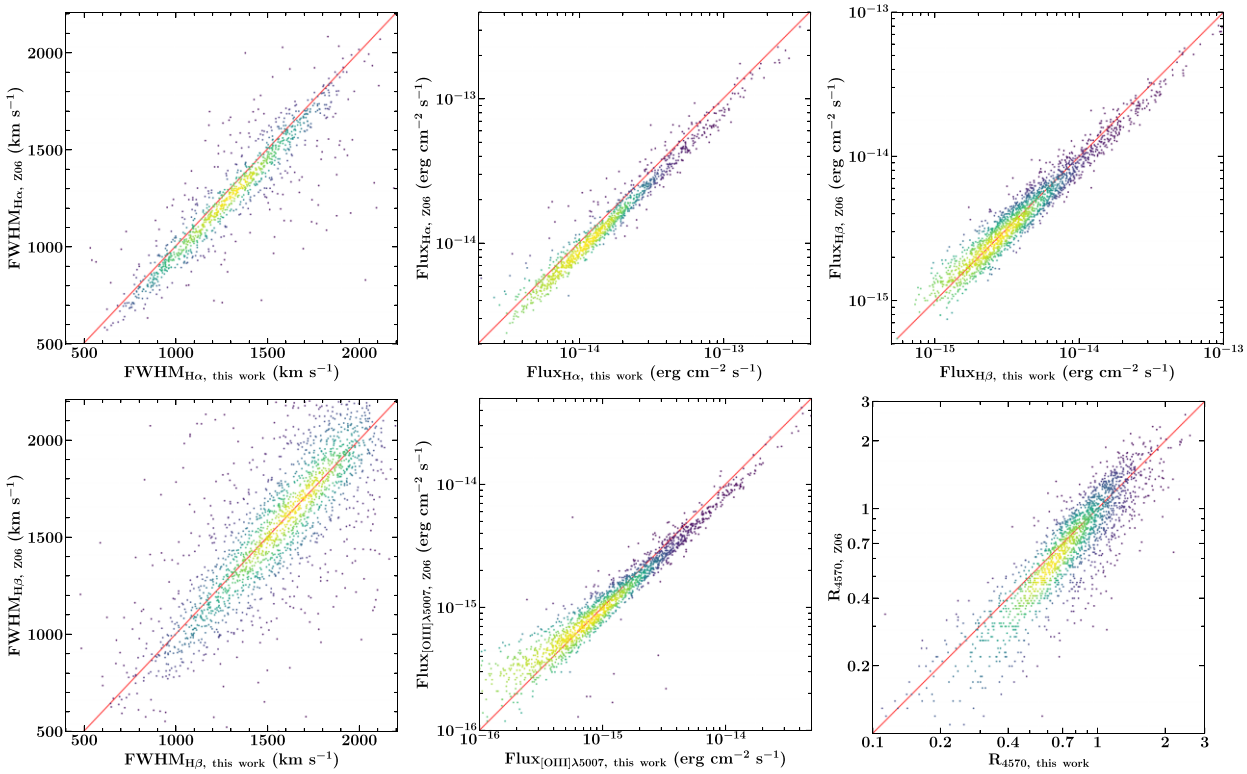

Figure 7. This plot shows the comparison of various spectral parameters obtained in this work and that published for SDSS-DR3 NLSy1 catalogue (Z06, Zhou et al. 2006). Other information are same as in Fig. 5.

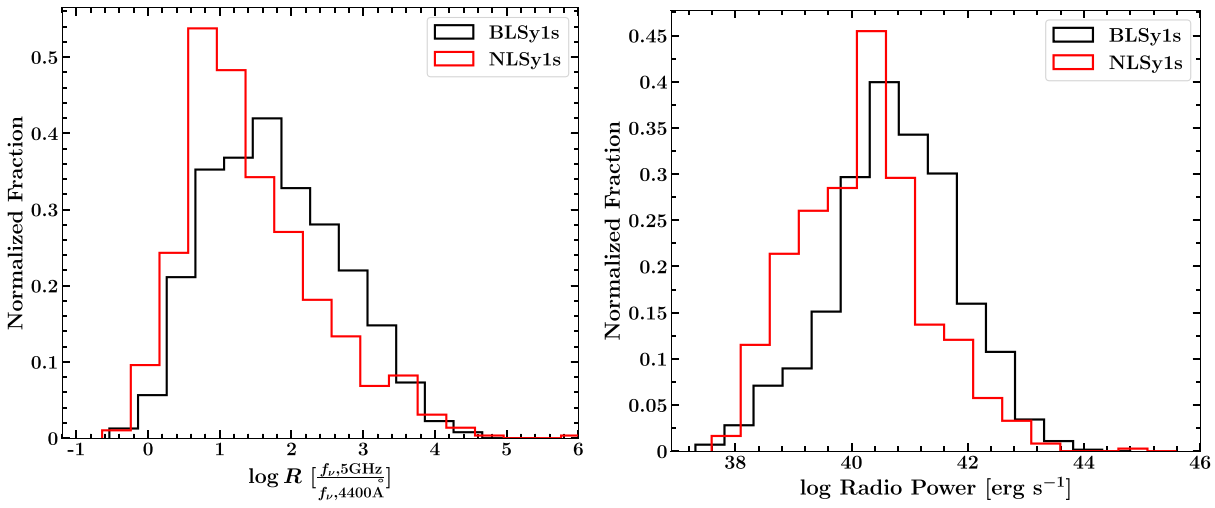

Figure 8. A comparison of the radio-loudness parameter (R, left) and k-corrected 1.4 GHz luminosity (right) for NLSy1 and BLSy1 galaxies.

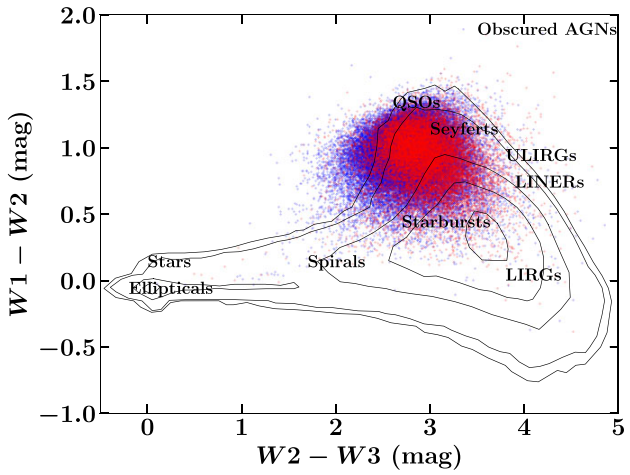

Figure 9. WISE colour–colour diagram for objects studied in this work. The plotted isodensity contours refer to WISE thermal sources and locations of various source classes are also highlighted. The acronyms QSOs, ULIRGs, LIRGs, and LINERs refer to quasars, ultraluminous infrared galaxies, luminous infrared galaxies, and low-ionization nuclear emission region galaxies, respectively. The contour data are adopted from Massaro et al. (2011).

$$\log(L_{[\mathrm{OIII}]}) = (12.44 \pm 0.22) + (0.675 \pm 0.005) \log L_{5100}. \quad (6)$$

All correlations were found $>5\sigma$ significant as also reported for SDSS-DR12 NLSy1 catalogue (Rakshit et al. 2017). These correlations between the continuum and emission line luminosities enable us to adopt the latter while estimating virial black hole masses for the cases where measuring the former is tedious, e.g. in blazars, galaxy-dominated low-luminosity sources, and Type 2 AGN (Zakamska et al. 2003; Greene & Ho 2005).

We show some of the parameters and physical properties of NLSy1 and BLSy1 sources estimated from the optical spectroscopic analysis in Fig. 11. The redshift distribution suggests an increase in number for both populations with redshift. At lower redshifts ($z < 0.5$), NLSy1s are more common whereas BLSy1 galaxies dominate at higher redshifts. Comparing the absolute B-band magnitudes, NLSy1s tend to appear a bit fainter ($\langle M_\mathrm{B} \rangle = -22.1$) with respect to

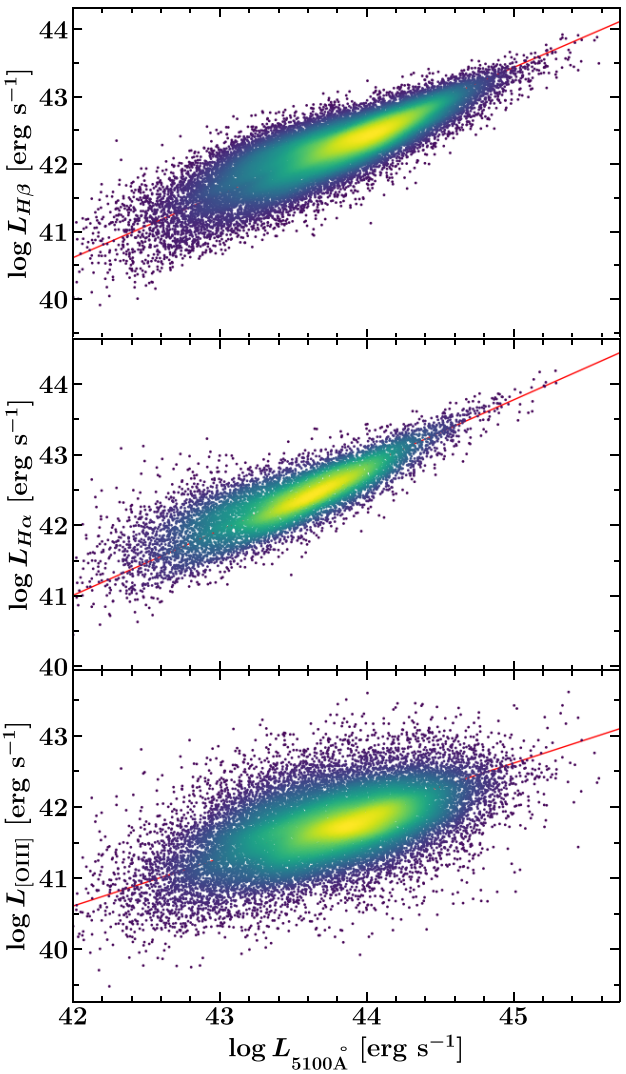

Figure 10. A comparison of the luminosity of the emission lines and 5100 Å continuum luminosity. The colour coding is done based on the number density of sources. The red line refers to the best-fitted correlation. See the text for details.

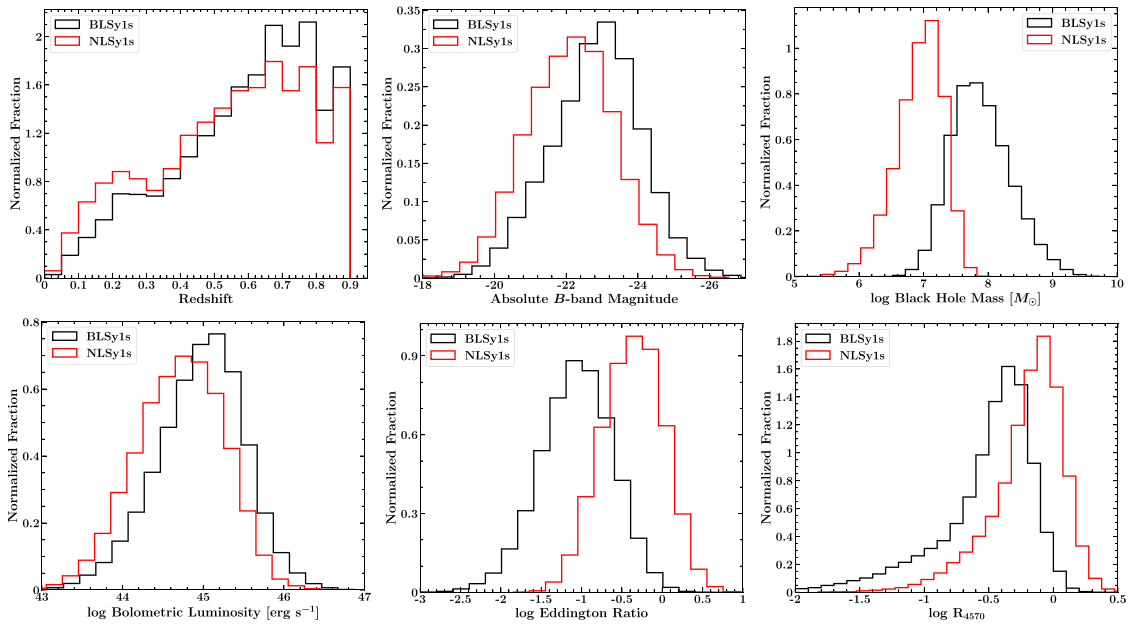

Figure 11. Comparisons of various optical spectroscopic parameters, measured/derived, for NLSy1 and BLSy1 sources. See the text for details.

BLSy1 objects ($\langle M_{\rm B}\rangle = -22.9$) though their dispersions are similar, $\sim$1.2 magnitudes. The black hole masses of NLSy1s ($\langle \log M_{\rm SE}\rangle = 6.98 \pm 0.37$, $M_\odot$) were also found to be lower than that of BLSy1 galaxies ($\langle \log M_{\rm SE}\rangle = 7.85 \pm 0.47$, $M_\odot$). This is likely due to the adopted FWHM of the broad Hβ line threshold which is used to compute $M_{\rm SE}$. Furthermore, since the differences in the bolometric luminosity distributions for both types of sources are not significant ($\langle \log L_{\rm bol}\rangle = 45.01, 44.74$ erg s^{-1}, for BLSy1 and NLSy1, respectively), a lower $M_{\rm SE}$ also implies a higher Eddington ratio or $R_{\rm Edd}$ for NLSy1 galaxies (Fig. 11, bottom middle panel). These results are consistent with those reported for SDSS-DR12 NLSy1 catalogue (Rakshit et al. 2017).

NLSy1 sources typically exhibit strong Fe II emission which is quantified using R_{4570} (e.g. Vanden Berk et al. 2001). We found the median R_{4570} parameter value to be 0.71 and 0.38 and 1σ dispersion to be 0.41 and 0.24 for NLSy1 and BLSy1 galaxies, respectively. These quantities are similar to those reported by Rakshit et al. (2017) and follow the same trend observed in earlier studies (cf. Bergeron & Kunth 1984; Vanden Berk et al. 2001; Zhou et al. 2006).

5.4 X-ray observations

We cross-matched our NLSy1 catalogue with the *Chandra* source catalogue v2.0 (Evans et al. 2010), the *eROSITA* Final Equitorial Depth Survey AGN catalogue (eFEDS; Liu et al. 2022), *XMM-Newton* serenditipious source catalogue (4XMM-DR12; Webb et al. 2020), and live *Swift*-X-ray Telescope Point Source Catalogue (Evans et al. 2023), in sequential order to identify X-ray emitting sources. Using a search radius of 5 arcsec, we found 567, 195, 979, and 819 matches, respectively. Some of these catalogues, e.g. eFEDS, provide spectral index measurements which we have used to determine its possible correlation with the accretion rate in Eddington units (cf. Risaliti, Young & Elvis 2009). No assumptions were made while considering spectral indices even though these X-ray surveys cover overlapping yet different energy bands. In Fig. 12, we show the variation of the photon index with Eddington ratio for sources detected with *Chandra* and *eROSITA* satellites. A positive correlation

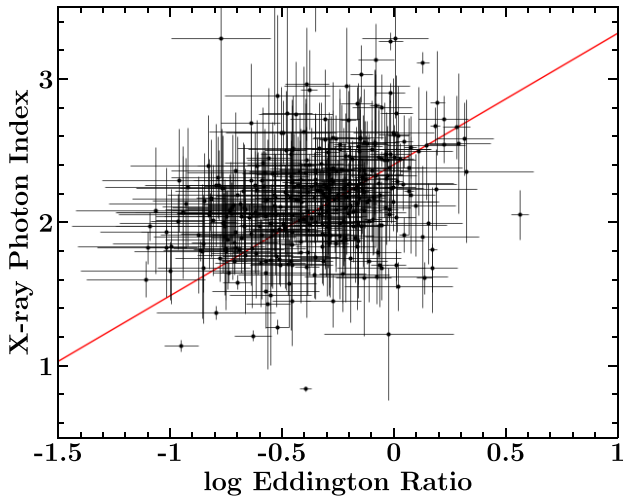

Figure 12. The variation of the X-ray photon index as a function of the Eddington ratio for NLSy1 galaxies detected with *Chandra* and *eROSITA* satellites. The red line corresponds to the best-fitted correlation.

is evident with the null hypothesis of no correlation is rejected at $>5\sigma$ confidence level. The best-fitted line slope ($m = 0.91 \pm 0.02$) is steeper than that reported in other studies (Risaliti, Young & Elvis 2009; Laurenti et al. 2022) which can be understood since no detailed X-ray data reduction was performed by us. Indeed, the X-ray spectra of NLSy1 sources exhibit several interesting features, e.g. soft excess below 2 keV (cf. Fabian et al. 2009), which should be properly taken into account while estimating spectral parameters.

5.5 Gamma-ray observations

The detection of variable gamma-ray emission from some of the radio-loud NLSy1 galaxies have provided strong evidence that even low black hole mass systems can launch powerful relativistic jets

(e.g. Abdo et al. 2009). To identify gamma-ray emitting NLSy1 galaxies in our sample, we considered the fourth data release of the fourth catalogue of gamma-ray sources detected by the *Fermi*-Large Area Telescope (4FGL-DR4; Ajello et al. 2022; Ballet et al. 2023). Adopting the counterpart positions given in this catalogue and using a search radius of 5 arcsec, we found 21 gamma-ray detected NLSy1 galaxies. The list is provided in Table 1. All sources previously known in the gamma-ray band except one are present in the list (Paliya 2019). The only missing object is the flat spectrum radio quasar GB6 J0937+5008 ($z = 0.28$) for which our spectral fitting analysis resulted in the broad H β line FWHM of 2350.2 ± 231.6 km s^{-1} thus classifying it as a broad-line AGN. Among the newly identified NLSy1s, nine sources are found to be gamma-ray emitters.

Among the broad-line sources, 45 are identified as gamma-ray emitters by cross-matching with the 4FGL-DR4 catalogue (Table 1). Interestingly, there are 10 objects that have absolute *B*-band magnitude $M_B > -23$, i.e. they are genuine Seyfert galaxies. This observation strengthens the idea that low-luminosity AGN can also host relativistic jets.

Table 1. The gamma-ray detected sources present in the NLSy1 and BLSy1 catalogues.

4FGL Name	4FGL Association	RA (deg.)	Decl. (deg.)	Redshift
	NLSy1 Galaxies			
J0001.5+2113	TXS 2358 + 209	0.38487	21.22672	0.438
J0010.6+2043	TXS 0007 + 205	2.61976	20.79716	0.597
J0014.3−0500	WISE J001420.42−045928.7	3.58514	− 4.99134	0.790
J0038.7−0204	3C 17	9.58555	− 2.12790	0.220
J0105.5+1912	TXS 0103 + 189	16.48014	19.20778	0.879
J0850.0+5108	SBS 0846 + 513	132.49155	51.14139	0.584
J0932.6+5306	S4 0929 + 53	143.17144	53.10938	0.597
J0933.5−0013	PMN J0933−0012	143.34596	− 0.18101	0.796
J0948.9+0022	PMN J0948+0022	147.23882	0.373753	0.585
J0949.2+1749	TXS 0946 + 181	147.41565	17.88037	0.692
J0958.0+3222	3C 232	149.58727	32.40061	0.530
J1127.8+3618	MG2 J112758+3620	171.99528	36.34121	0.884
J1305.3+5118	IERS B1303 + 515	196.34476	51.27785	0.787
J1331.0+3032	3C 286	202.78456	30.50913	0.85
J1443.1+4728	B3 1441 + 476	220.82733	47.43241	0.705
J1505.0+0326	PKS 1502 + 036	226.27698	3.441895	0.407
J1520.5+4209	B3 1518 + 423	230.16538	42.18644	0.485
J1639.2+4129	MG4 J163918+4127	249.81587	41.47603	0.690
J1644.9+2620	MG2 J164443+2618	251.17722	26.32035	0.144
J2118.0+0019	PMN J2118+0013	319.57249	0.22132	0.463
J2118.8−0723	TXS 2116 − 077	319.72068	− 7.54098	0.260
	BLSy1 Galaxies			
J0059.2+0006	PKS 0056 − 00	14.77297	0.11434	0.719
J0112.1−0321	TXS 0110 − 037	18.16305	− 3.47855	0.772
J0121.8+1147	PKS 0119 + 11	20.42330	11.83067	0.571
J0136.8+2032	GB6 J0136+2028	24.13413	20.47153	0.557
J0203.7+3042	IVS B0200 + 30A	30.93447	30.71052	0.76
J0758.1+1134	TXS 0755 + 117	119.53189	11.61279	0.568
J0814.4+2941	RX J0814.4+2941	123.60795	29.68770	0.373
J0827.8+5221	TXS 0824 + 524	126.97374	52.29953	0.338
J0840.8+1317	3C 207	130.19828	13.20654	0.68
J0914.4+0249	PKS 0912 + 029	138.65796	2.76645	0.426
J0924.0+2816	B2 0920 + 28	140.96468	28.25698	0.744
J0937.1+5008	GB6 J0937+5008	144.30135	50.14782	0.275
J0943.7+6137	GB6 B0940 + 6149	146.08517	61.59726	0.791
J0945.2+5200	TXS 0941 + 522	146.21729	52.04281	0.5
J0956.7+2516	OK 290	149.20783	25.25446	0.708
J1014.8+2257	OL 220	153.69611	23.02127	0.566
J1015.6+5553	TXS 1012 + 560	153.93508	55.85017	0.678
J1036.2+2202	OL 256	159.13741	22.05339	0.595
J1059.5+2057	MG2 J105938+2057	164.91266	20.95608	0.393
J1102.6+5251	GB6 J1102+5249	165.70771	52.83685	0.69
J1102.9+3014	B2 1100 + 30B	165.80542	30.24521	0.384
J1153.4+4931	4C + 49.22	178.35194	49.51910	0.333
J1159.5+2914	Ton 599	179.88265	29.24551	0.724
J1209.8+1810	MG1 J120953+1809	182.46566	18.16857	0.845
J1224.9+2122	4C + 21.35	186.22691	21.37955	0.433
J1257.8+3228	ON 393	194.48866	32.49157	0.805
J1332.2+4722	B3 1330 + 476	203.18850	47.37296	0.669
J1334.5+5634	TXS 1332 + 567	203.65616	56.52997	0.342

Table 1 – *continued*

4FGL Name	4FGL Association	RA (deg.)	Decl. (deg.)	Redshift
J1350.8+3033	B2 1348 + 30B	207.71972	30.58155	0.712
J1357.1+1921	4C + 19.44	209.26846	19.31872	0.719
J1422.5+3223	OQ 334	215.62657	32.38623	0.681
J1430.5+3647	TXS 1428 + 370	217.66911	36.81775	0.567
J1443.1+5201	3C 303	220.76150	52.02701	0.141
J1524.2+1523	MC3 1522 + 155	231.17338	15.35585	0.630
J1549.5+0236	PKS 1546 + 027	237.37265	2.61697	0.414
J1604.6+5714	GB6 J1604+5714	241.15563	57.24351	0.721
J1608.3+4012	B2 1606 + 40	242.09232	40.20498	0.628
J1637.7+4717	4C + 47.44	249.43805	47.29273	0.735
J1642.9+3948	3C 345	250.74503	39.81029	0.593
J1659.0+2627	4C + 26.51	254.85061	26.49360	0.793
J1706.9+4543	4C + 45.34	256.82397	45.60292	0.645
		BLSy1 Galaxies		
J2157.0+1002	MC2 2154 + 100	329.30356	10.24024	0.761
J2301.0−0158	PKS B2258 − 022	345.28322	− 1.96796	0.777
J2334.2+0736	TXS 2331 + 073	353.55344	7.60764	0.401
J2352.9+3031	MG3 J235254+3030	358.22795	30.50603	0.876

6 SUMMARY

In this work, we have carried out a detailed analysis of >2 million SDSS spectra using the publicly available software BADASS to identify NLSy1 galaxies in the latest SDSS-DR17. By reproducing the Balmer emission lines with the Lorentzian profile and also adopting the multi-component continuum fitting which includes contributions from the optical Fe II emission, host galaxy, and nuclear power-law AGN radiation, we identified 22656 NLSy1 galaxies with broad H β emission line FWHM <2000 km s^{-1} within uncertainties. Furthermore, >75 per cent of these objects are found to be low-luminosity AGN with $M_{\rm B} > -23$ (Schmidt & Green 1983). This exercise also led to a new catalogue of 52 273 BLSy1 galaxies. Comparing with previous works (Zhou et al. 2006; Rakshit et al. 2017), we found >80 per cent of their NLSy1s to be present in our catalogue and the corresponding optical spectroscopic parameters were also found to be comparable, thereby supporting the robustness of our analysis procedure and results. Based on the estimated parameters and derived quantities, e.g. $M_{\rm SE}$, we confirm earlier findings of NLSy1s being AGN powered by rapidly accreting low-mass black holes and the steepening of the X-ray spectrum with increasing Eddington rate (cf. Boller, Brandt & Fink 1996). We conclude that with the advent of the ongoing and upcoming wide-field, multiwavelength sky surveys, e.g. VLASS, this new catalogue of NLSy1 galaxies will enable us to explore the physics of this enigmatic class of AGN in an unprecedented detail hence sowing the seeds for their future observations with the next-generation of giant telescopes.

The catalogue is made public at https://www.ucm.es/blazars/seyfert and also provided as a supplementary material of this article.

ACKNOWLEDGEMENTS

We are grateful to the referee for constructive criticism, which has helped improve the paper. VSP is grateful to Remington Sexton for a fruitful discussion on the use of BADASS software. AD is thankful for the support of the Ramón y Cajal programme from the Spanish MINECO, Proyecto PID2021-126536OA-I00 funded by MCIN / AEI / 10.13039/501100011033, and Proyecto PR44/21-29915 funded by the Santander Bank and Universidad Complutense de Madrid.

Funding for the Sloan Digital Sky Survey IV was provided by the Alfred P. Sloan Foundation, the U.S. Department of Energy Office of Science, and the Participating Institutions. SDSS-IV acknowledges support and resources from the Center for High-Performance Computing at the University of Utah. The SDSS web site is www.sdss.org.

SDSS-IV is managed by the Astrophysical Research Consortium for the Participating Institutions of the SDSS Collaboration including the Brazilian Participation Group, the Carnegie Institution for Science, Carnegie Mellon University, the Chilean Participation Group, the French Participation Group, Harvard-Smithsonian Center for Astrophysics, Instituto de Astrofísica de Canarias, The Johns Hopkins University, Kavli Institute for the Physics and Mathematics of the Universe (IPMU) / University of Tokyo, the Korean Participation Group, Lawrence Berkeley National Laboratory, Leibniz Institut für Astrophysik Potsdam (AIP), Max-Planck-Institut für Astronomie (MPIA Heidelberg), Max-Planck-Institut für Astrophysik (MPA Garching), Max-Planck-Institut für Extraterrestrische Physik (MPE), National Astronomical Observatories of China, New Mexico State University, New York University, University of Notre Dame, Observatário Nacional / MCTI, The Ohio State University, Pennsylvania State University, Shanghai Astronomical Observatory, United Kingdom Participation Group,Universidad Nacional Autónoma de México, University of Arizona, University of Colorado Boulder, University of Oxford, University of Portsmouth, University of Utah, University of Virginia, University of Washington, University of Wisconsin, Vanderbilt University, and Yale University.

This publication makes use of data products from the Wide-field Infrared Survey Explorer, which is a joint project of the University of California, Los Angeles, and the Jet Propulsion Laboratory/California Institute of Technology, funded by the National Aeronautics and Space Administration.

This research has made use of the NASA/IPAC Extragalactic Database (NED), which is operated by the Jet Propulsion Laboratory, California Institute of Technology, under contract with the National Aeronautics and Space Administration. Part of this work is based on archival data, software or online services provided by the Space Science Data Center (SSDC). This research has made use of NASA's Astrophysics Data System Bibliographic Services.

This work made use of data supplied by the UK Swift Science Data Centre at the University of Leicester. This research has made

use of data obtained from the Chandra Source Catalog, provided by the Chandra X-ray Center (CXC) as part of the Chandra Data Archive.

DATA AVAILABILITY

All of the multiwavelength data used in this article are publicly available at their respective data archives, e.g. SDSS-DR17 (https://skyserver.sdss.org/dr17/). The software used to analyse the SDSS spectra is publicly available (https://github.com/remingtonsexton/BADASS3).

REFERENCES

Abdo A. A. et al., 2009, ApJ, 707, L142
Ajello M. et al., 2022, ApJS, 263, 24
Assef R. J., Stern D., Noirot G., Jun H. D., Cutri R. M., Eisenhardt P. R. M., 2018, ApJS, 234, 23
Ballet J., Bruel P., Burnett T. H., Lott B., The Fermi-LAT Collaboration, 2023, preprint (arXiv:2307.12546)
Bergeron J., Kunth D., 1984, MNRAS, 207, 263
Berton M. et al., 2018, A&A, 614, A87
Blanton M. R. et al., 2017, AJ, 154, 28
Boller T., Brandt W. N., Fink H., 1996, A&A, 305, 53
Boroson T. A., 2002, ApJ, 565, 78
Boroson T. A., Green R. F., 1992, ApJS, 80, 109
Cappellari M., 2017, MNRAS, 466, 798
Cardelli J. A., Clayton G. C., Mathis J. S., 1989, ApJ, 345, 245
Cracco V., Ciroi S., Berton M., Di Mille F., Foschini L., La Mura G., Rafanelli P., 2016, MNRAS, 462, 1256
Decarli R., Dotti M., Fontana M., Haardt F., 2008, MNRAS, 386, L15
Dietrich M., Appenzeller I., Vestergaard M., Wagner S. J., 2002, ApJ, 564, 581
Domínguez A. et al., 2013, ApJ, 763, 145
Du P., Wang J.-M., 2019, ApJ, 886, 42
Evans I. N. et al., 2010, ApJS, 189, 37
Evans P. A., Page K. L., Beardmore A. P., Eyles-Ferris R. A. J., Osborne J. P., Campana S., Kennea J. A., Cenko S. B., 2023, MNRAS, 518, 174
Fabian A. C. et al., 2009, Nature, 459, 540
Foreman-Mackey D., Hogg D. W., Lang D., Goodman J., 2013, PASP, 125, 306
Frederick S. et al., 2021, ApJ, 920, 56
Goad M. R., Korista K. T., Ruff A. J., 2012, MNRAS, 426, 3086
Goodrich R. W., 1989, ApJ, 342, 224
Greene J. E., Ho L. C., 2005, ApJ, 630, 122
Grupe D., Mathur S., 2004, ApJ, 606, L41
Grupe D., Komossa S., Leighly K. M., Page K. L., 2010, ApJS, 187, 64
Ivezić Ž. et al., 2019, ApJ, 873, 111
Jordi K., Grebel E. K., Ammon K., 2006, A&A, 460, 339
Jun H. D. et al., 2015, ApJ, 806, 109
Kara E., García J. A., Lohfink A., Fabian A. C., Reynolds C. S., Tombesi F., Wilkins D. R., 2017, MNRAS, 468, 3489
Kellermann K. I., Sramek R., Schmidt M., Shaffer D. B., Green R., 1989, AJ, 98, 1195
Komossa S., Voges W., Xu D., Mathur S., Adorf H.-M., Lemson G., Duschl W. J., Grupe D., 2006, AJ, 132, 531
Komossa S., Xu D., Zhou H., Storchi-Bergmann T., Binette L., 2008, ApJ, 680, 926
Lacy M. et al., 2020, PASP, 132, 035001
Laurenti M. et al., 2022, A&A, 657, A57
Leighly K. M., 1999a, ApJS, 125, 297
Leighly K. M., 1999b, ApJS, 125, 317
Liu T. et al., 2022, A&A, 661, A5
Lyke B. W. et al., 2020, ApJS, 250, 8
Marziani P., Sulentic J. W., Zwitter T., Dultzin-Hacyan D., Calvani M., 2001, ApJ, 558, 553
Massaro F., D'Abrusco R., Ajello M., Grindlay J. E., Smith H. A., 2011, ApJ, 740, L48
Mathur S., 2000, MNRAS, 314, L17
McLure R. J., Dunlop J. S., 2004, MNRAS, 352, 1390
Osterbrock D. E., Pogge R. W., 1985, ApJ, 297, 166
Paliya V. S., 2019, J. Astrophys. Astron., 40, 39
Paliya V. S., Ajello M., Rakshit S., Mandal A. K., Stalin C. S., Kaur A., Hartmann D., 2018, ApJ, 853, L2
Paliya V. S. et al., 2020, ApJ, 892, 133
Pâris I. et al., 2017, A&A, 597, A79
Parker M. L. et al., 2014, MNRAS, 443, 1723
Peterson B. M. et al., 2000, ApJ, 542, 161
Predehl P. et al., 2021, A&A, 647, A1
Rakshit S., Stalin C. S., Chand H., Zhang X.-G., 2017, ApJS, 229, 39
Richards G. T. et al., 2006, ApJS, 166, 470
Risaliti G., Young M., Elvis M., 2009, ApJ, 700, L6
Schlafly E. F., Finkbeiner D. P., 2011, ApJ, 737, 103
Schmidt M., Green R. F., 1983, ApJ, 269, 352
Sexton R. O., Matzko W., Darden N., Canalizo G., Gorjian V., 2021, MNRAS, 500, 2871
Sexton R. O., Secrest N. J., Johnson M. C., Dorland B. N., 2022, ApJS, 260, 33
Shen Y., 2013, Bull. Astron. Soc. India, 41, 61
Shen Y. et al., 2011, ApJS, 194, 45
Singh V., Chand H., 2018, MNRAS, 480, 1796
Sulentic J. W., Marziani P., Dultzin-Hacyan D., 2000, ARA&A, 38, 521
Sulentic J. W., Marziani P., Zamanov R., Bachev R., Calvani M., Dultzin-Hacyan D., 2002, ApJ, 566, L71
Vanden Berk D. E. et al., 2001, AJ, 122, 549
Vazdekis A., Koleva M., Ricciardelli E., Röck B., Falcón-Barroso J., 2016, MNRAS, 463, 3409
Véron-Cetty M. P., Joly M., Véron P., 2004, A&A, 417, 515
Vestergaard M., Peterson B. M., 2006, ApJ, 641, 689
Vestergaard M., Wilkes B. J., 2001, ApJS, 134, 1
Webb N. A. et al., 2020, A&A, 641, A136
White R. L., Becker R. H., Helfand D. J., Gregg M. D., 1997, ApJ, 475, 479
Williams R. J., Pogge R. W., Mathur S., 2002, AJ, 124, 3042
Wright E. L. et al., 2010, AJ, 140, 1868
Wu Q., Shen Y., 2022, ApJS, 263, 42
Xu D., Komossa S., Zhou H., Lu H., Li C., Grupe D., Wang J., Yuan W., 2012, AJ, 143, 83
Yan L. et al., 2013, AJ, 145, 55
Yuan W., Zhou H. Y., Komossa S., Dong X. B., Wang T. G., Lu H. L., Bai J. M., 2008, ApJ, 685, 801
Zakamska N. L. et al., 2003, AJ, 126, 2125
Zhou H., Wang T., Yuan W., Lu H., Dong X., Wang J., Lu Y., 2006, ApJS, 166, 128

SUPPORTING INFORMATION

Supplementary data are available at *MNRAS* online.

Catalog_New.fits

Please note: Oxford University Press is not responsible for the content or functionality of any supporting materials supplied by the authors. Any queries (other than missing material) should be directed to the corresponding author for the article.

APPENDIX A: DETAILS OF THE CATALOGUE FITS FILE

We provide the full description of the fits catalogue below in Table A1.

Table A1. The format of the FITS catalogue.

Column	Format	Units	Description
SDSS_NAME	STRING		SDSS DR17 designation (J2000)
P-M-F	STRING		Spectroscopic plate number, MJD, and fibre number
RA	DOUBLE	degree	Right ascension (J2000)
DEC	DOUBLE	degree	Declination (J2000)
Z	DOUBLE		Spectroscopic redshift
M_B	DOUBLE		Absolute *B*-band magnitude
BR_H_ALPHA_EW	DOUBLE	(Å)	Rest-frame equivalent-width of the broad H α emission line
BR_H_ALPHA_EW_ERR	DOUBLE	(Å)	Uncertainty in rest-frame equivalent-width of the broad H α emission line
BR_H_ALPHA_FLUX	DOUBLE	(erg cm^{-2} s^{-1})	Flux of the broad H α emission line on logarithmic scale
BR_H_ALPHA_FLUX_ERR	DOUBLE	(erg cm^{-2} s^{-1})	Uncertainty in the logarithmic-scaled flux of the broad emission line
BR_H_ALPHA_FWHM	DOUBLE	(km s^{-1})	FWHM of the broad H α emission line
BR_H_ALPHA_FWHM_ERR	DOUBLE	(km s^{-1})	Uncertainty in the FWHM of the broad H α emission line
BR_H_ALPHA_LUM	DOUBLE	(erg s^{-1})	Luminosity of the broad H α emission line on logarithmic scale
BR_H_ALPHA_LUM_ERR	DOUBLE	(erg s^{-1})	Uncertainty in the logarithmic-scaled luminosity of the broad H α emission line
BR_H_ALPHA_SNR	DOUBLE		S/N ratio of the broad H α emission line
BR_H_BETA_EW	DOUBLE	(Å)	Rest-frame equivalent-width of the broad H β emission line
BR_H_BETA_EW_ERR	DOUBLE	(Å)	Uncertainty in rest-frame equivalent-width of the broad H β emission line
BR_H_BETA_FLUX	DOUBLE	(erg cm^{-2} s^{-1})	Flux of the broad H β emission line on logarithmic scale
BR_H_BETA_FLUX_ERR	DOUBLE	(erg cm^{-2} s^{-1})	Uncertainty in the logarithmic-scaled flux of the broad H β emission line
BR_H_BETA_FWHM	DOUBLE	(km s^{-1})	FWHM of the broad H β emission line
BR_H_BETA_FWHM_ERR	DOUBLE	(km s^{-1})	Uncertainty in the FWHM of the broad H β emission line
BR_H_BETA_LUM	DOUBLE	(erg s^{-1})	Luminosity of the broad H β emission line (erg s^{-1}) on logarithmic scale
BR_H_BETA_LUM_ERR	DOUBLE	(erg s^{-1})	Uncertainty in the logarithmic-scaled luminosity of the broad H β emission line
BR_H_BETA_SNR	DOUBLE		S/N ratio of the broad H β emission line
NA_H_ALPHA_EW	DOUBLE	Å	Rest-frame equivalent-width of the narrow H α emission line
NA_H_ALPHA_EW_ERR	DOUBLE	(Å)	Uncertainty in rest-frame equivalent-width of the narrow H α emission line
NA_H_ALPHA_FLUX	DOUBLE	(erg cm^{-2} s^{-1})	Flux of the narrow H α emission line on logarithmic scale
NA_H_ALPHA_FLUX_ERR	DOUBLE	(erg cm^{-2} s^{-1})	Uncertainty in the logarithmic-scaled flux of the narrow H α emission line
NA_H_ALPHA_FWHM	DOUBLE	(km s^{-1})	FWHM of the narrow H α emission line
NA_H_ALPHA_FWHM_ERR	DOUBLE	(km s^{-1})	Uncertainty in the FWHM of the narrow H α emission line
NA_H_ALPHA_LUM	DOUBLE	(erg s^{-1})	Luminosity of the narrow H α emission line (erg s^{-1}) on logarithmic scale
NA_H_ALPHA_LUM_ERR	DOUBLE	(erg s^{-1})	Uncertainty in the logarithmic-scaled luminosity of the narrow H α emission line
NA_H_ALPHA_SNR	DOUBLE		S/N ratio of the narrow H α emission line
NA_H_BETA_EW	DOUBLE	(Å)	Rest-frame equivalent-width of the narrow H β emission line
NA_H_BETA_EW_ERR	DOUBLE	(Å)	Uncertainty in rest-frame equivalent-width of the narrow H β emission line
NA_H_BETA_FLUX	DOUBLE	(erg cm^{-2} s^{-1})	Flux of the narrow H β emission line on logarithmic scale
NA_H_BETA_FLUX_ERR	DOUBLE	(erg cm^{-2} s^{-1})	Uncertainty in the logarithmic-scaled flux of the narrow H β emission line
NA_H_BETA_FWHM	DOUBLE	(km s^{-1})	FWHM of the narrow H β emission line
NA_H_BETA_FWHM_ERR	DOUBLE	(km s^{-1})	Uncertainty in the FWHM of the narrow H β emission line
NA_H_BETA_LUM	DOUBLE	(erg s^{-1})	Luminosity of the narrow H β emission line (erg s^{-1}) on logarithmic scale
NA_H_BETA_LUM_ERR	DOUBLE	(erg s^{-1})	Uncertainty in the logarithmic-scaled luminosity of the narrow H β emission line
NA_H_BETA_SNR	DOUBLE		S/N ratio of the narrow H β emission line
NA_OIII_4960_EW	DOUBLE	(Å)	Rest-frame equivalent-width of the narrow [O III] λ4959 emission line
NA_OIII_4960_EW_ERR	DOUBLE	(Å)	Uncertainty in rest-frame equivalent-width of the narrow [O III] λ4959 emission line
NA_OIII_4960_FLUX	DOUBLE	(erg cm^{-2} s^{-1})	Flux of the narrow [O III] λ4959 emission line on logarithmic scale
NA_OIII_4960_FLUX_ERR	DOUBLE	(erg cm^{-2} s^{-1})	Uncertainty in the logarithmic-scaled flux of the narrow [O III] λ4959 emission line
NA_OIII_4960_FWHM	DOUBLE	(km s^{-1})	FWHM of the narrow [O III] λ4959 emission line
NA_OIII_4960_FWHM_ERR	DOUBLE	(km s^{-1})	Uncertainty in the FWHM of the narrow [O III] λ4959 emission line
NA_OIII_4960_LUM	DOUBLE	(erg s^{-1})	Luminosity of the narrow [O III] λ4959 emission line on logarithmic scale
NA_OIII_4960_LUM_ERR	DOUBLE	(erg s^{-1})	Uncertainty in the logarithmic-scaled luminosity of the narrow [O III] λ4959 emission line
NA_OIII_4960_SNR	DOUBLE		S/N ratio of the narrow [O III] λ4959 emission line
NA_OIII_5007_EW	DOUBLE	(Å)	Rest-frame equivalent-width of the narrow [O III] λ5007 emission line
NA_OIII_5007_EW_ERR	DOUBLE	(Å)	Uncertainty in rest-frame equivalent-width of the narrow [O III] λ5007 emission line
NA_OIII_5007_FLUX	DOUBLE	(erg cm^{-2} s^{-1})	Flux of the narrow [O III] λ5007 emission line on logarithmic scale
NA_OIII_5007_FLUX_ERR	DOUBLE	(erg cm^{-2} s^{-1})	Uncertainty in the logarithmic-scaled flux of the narrow [O III] λ5007 emission line
NA_OIII_5007_FWHM	DOUBLE	(km s^{-1})	FWHM of the narrow [O III] λ5007 emission line
NA_OIII_5007_FWHM_ERR	DOUBLE	(km s^{-1})	Uncertainty in the FWHM of the narrow [O III] λ5007 emission line
NA_OIII_5007_LUM	DOUBLE	(erg s^{-1})	Luminosity of the narrow [O III] λ5007 emission line (erg s^{-1}) on logarithmic scale
NA_OIII_5007_LUM_ERR	DOUBLE	(erg s^{-1})	Uncertainty in the logarithmic-scaled luminosity of the narrow [O III] λ5007 emission line
NA_OIII_5007_SNR	DOUBLE		S/N ratio of the narrow [O III] λ5007 emission line
NA_NII_6549_EW	DOUBLE	(Å)	Rest-frame equivalent-width of the narrow [N II] λ6549 emission line

Table A1 – *continued*

Column	Format	Units	Description
NA_NII_6549_EW_ERR	DOUBLE	(Å)	Uncertainty in rest-frame equivalent-width of the narrow [N II] λ6549 emission line
NA_NII_6549_FLUX	DOUBLE	(erg cm^{-2} s^{-1})	Flux of the narrow [N II] λ6549 emission line on logarithmic scale
NA_NII_6549_FLUX_ERR	DOUBLE	(erg cm^{-2} s^{-1})	Uncertainty in the logarithmic-scaled flux of the narrow [N II] λ6549 emission line
NA_NII_6549_FWHM	DOUBLE	(km s^{-1})	FWHM of the narrow [N II] λ6549 emission line
NA_NII_6549_FWHM_ERR	DOUBLE	(km s^{-1})	Uncertainty in the FWHM of the narrow [N II] λ6549 emission line
NA_NII_6549_LUM	DOUBLE	(erg s^{-1})	Luminosity of the narrow [N II] λ6549 emission line (erg s^{-1}) on logarithmic scale
NA_NII_6549_LUM_ERR	DOUBLE	(erg s^{-1})	Uncertainty in the logarithmic-scaled luminosity of the narrow [N II] λ6549 emission line
NA_NII_6549_SNR	DOUBLE		S/N ratio of the narrow [N II] λ6549 emission line
NA_NII_6585_EW	DOUBLE	(Å)	Rest-frame equivalent-width of the narrow [N II] λ6585 emission line
NA_NII_6585_EW_ERR	DOUBLE	(Å)	Uncertainty in rest-frame equivalent-width of the narrow [N II] λ6585 emission line
NA_NII_6585_FLUX	DOUBLE	(erg cm^{-2} s^{-1})	Flux of the narrow [N II] λ6585 emission line on logarithmic scale
NA_NII_6585_FLUX_ERR	DOUBLE	(erg cm^{-2} s^{-1})	Uncertainty in the logarithmic-scaled flux of the narrow [N II] λ6585 emission line
NA_NII_6585_FWHM	DOUBLE	(km s^{-1})	FWHM of the narrow [N II] λ6585 emission line
NA_NII_6585_FWHM_ERR	DOUBLE	(km s^{-1})	Uncertainty in the FWHM of the narrow [N II] λ6585 emission line
NA_NII_6585_LUM	DOUBLE	(erg s^{-1})	Luminosity of the narrow [N II] λ6585 emission line (erg s^{-1}) on logarithmic scale
NA_NII_6585_LUM_ERR	DOUBLE	(erg s^{-1})	Uncertainty in the logarithmic-scaled luminosity of the narrow [N II] λ6585 emission line
NA_NII_6585_SNR	DOUBLE		S/N ratio of the narrow [N II] λ6585 emission line
NA_SII_6718_EW	DOUBLE	(Å)	Rest-frame equivalent-width of the narrow [S II] λ6718 emission line
NA_SII_6718_EW_ERR	DOUBLE	(Å)	Uncertainty in rest-frame equivalent-width of the narrow [S II] λ6718 emission line
NA_SII_6718_FLUX	DOUBLE	(erg cm^{-2} s^{-1})	Flux of the narrow [S II] λ6718 emission line (erg cm^{-2} s^{-1}) on logarithmic scale
NA_SII_6718_FLUX_ERR	DOUBLE	(erg cm^{-2} s^{-1})	Uncertainty in the logarithmic-scaled flux of the narrow [S II] λ6718 emission line
NA_SII_6718_FWHM	DOUBLE	(km s^{-1})	FWHM of the narrow [S II] λ6718 emission line
NA_SII_6718_FWHM_ERR	DOUBLE	(km s^{-1})	Uncertainty in the FWHM of the narrow [S II] λ6718 emission line
NA_SII_6718_LUM	DOUBLE	(erg s^{-1})	Luminosity of the narrow [S II] λ6718 emission line on logarithmic scale
NA_SII_6718_LUM_ERR	DOUBLE	(erg s^{-1})	Uncertainty in the logarithmic-scaled luminosity of the narrow [S II] λ6718 emission line
NA_SII_6718_SNR	DOUBLE		S/N ratio of the narrow [S II] λ6718 emission line
NA_SII_6732_EW	DOUBLE	(Å)	Rest-frame equivalent-width of the narrow [S II] λ6732 emission line
NA_SII_6732_EW_ERR	DOUBLE	(Å)	Uncertainty in rest-frame equivalent-width of the narrow [S II] λ6732 emission line
NA_SII_6732_FLUX	DOUBLE	(erg cm^{-2} s^{-1})	Flux of the narrow [S II] λ6732 emission line on logarithmic scale
NA_SII_6732_FLUX_ERR	DOUBLE	(erg cm^{-2} s^{-1})	Uncertainty in the logarithmic-scaled flux of the narrow [S II] λ6732 emission line
NA_SII_6732_FWHM	DOUBLE	(km s^{-1})	FWHM of the narrow [S II] λ6732 emission line
NA_SII_6732_FWHM_ERR	DOUBLE	(km s^{-1})	Uncertainty in the FWHM of the narrow [S II] λ6732 emission line
NA_SII_6732_LUM	DOUBLE	(erg s^{-1})	Luminosity of the narrow [S II] λ6732 emission line on logarithmic scale
NA_SII_6732_LUM_ERR	DOUBLE	(erg s^{-1})	Uncertainty in the logarithmic-scaled luminosity of the narrow [S II] λ6732 emission line
NA_SII_6732_SNR	DOUBLE		S/N ratio of the narrow [S II] λ6732 emission line
L_CONT_AGN_5100	DOUBLE	(erg s^{-1})	Rest-frame continuum luminosity at 5100 Å (erg s^{-1}) on logarithmic scale
L_CONT_AGN_5100_ERR	DOUBLE	(erg s^{-1})	Uncertainty in the logarithmic-scaled continuum luminosity at 5100 Å
R4570	DOUBLE		Fe II strength
M_BH	DOUBLE	($M_\odot$)	Logarithmic-scaled single epoch black hole mass estimated using H β emission line parameters
M_BH_ERR	DOUBLE	($M_\odot$)	Uncertainty in the logarithmic-scaled black hole mass estimated using H β emission line parameters
L_BOL	DOUBLE	(erg s^{-1})	Bolometric luminosity on logarithmic scale
L_BOL_ERR	DOUBLE	(erg s^{-1})	Uncertainty in the logarithmic-scaled bolometric luminosity
R_EDD	DOUBLE		Eddington ratio on logarithmic scale
R_EDD_ERR	DOUBLE		Uncertainty in the logarithmic-scaled Eddington ratio
RL	DOUBLE		radio-loudness parameter on logarithmic scale

This paper has been typeset from a TEX/LATEX file prepared by the author.